Liquid water in the Martian mid-crust

Vashan Wright[a,1] (iD), Matthias Morzfeld[a] (iD), and Michael Manga[b] (iD)

Large volumes of liquid water transiently existed on the surface of Mars more than 3 billion years ago. Much of this water is hypothesized to have been sequestered in the subsurface or lost to space. We use rock physics models and Bayesian inversion to identify combinations of lithology, liquid water saturation, porosity, and pore shape consistent with the constrained mid-crust ($\sim$11.5 to 20 km depths) seismic velocities and gravity near the InSight lander. A mid-crust composed of fractured igneous rocks saturated with liquid water best explains the existing data. Our results have implications for understanding Mars' water cycle, determining the fates of past surface water, searching for past or extant life, and assessing in situ resource utilization for future missions.

Mars | water | planetary geophysics | InSight

Liquid water existed at least episodically on Mars in rivers (1), lakes (1), oceans (2), and aquifers (3) during the Noachian and Hesperian, more than 3 billion years ago. Mars lost its ability to host persistent bodies of liquid water on its surface after the planet lost most of its atmosphere during this time period (4). The ancient surface water may have been incorporated in minerals (5), buried as ice, sequestered as liquid in deep aquifers, or lost to space (4).

Geophysical measurements have the potential to identify water in the deep subsurface. For example, seismic velocities derived from ground motion measured by the InSight (interior exploration using seismic investigations, geodesy, and heat transport) mission and interpreted with rock physics models have been used to constrain water distribution to depths of 20 km beneath the InSight lander, Elysium Planitia. The shear V_s and compression V_p wave velocities within the upper 300 m beneath InSight are consistent with a dry crust composed of minimally cemented (<2% of the pores) sediments (6). V_s in the upper 8 km beneath InSight is lower than expected for an ice-saturated cryosphere (7), though V_s may be higher elsewhere (8, 9). Kilburn et al. (7) argue that the crust between 8 and 20 km beneath InSight is a) mafic and highly porous or b) felsic and less porous, but with V_s alone, could not determine whether the fractures contain liquid water.

We assess whether V_s (10–13), V_p (12), and bulk density ρ_b (14) data (Table 1) are consistent with liquid water-saturated pores in the mid-crust (11.5 ± 3.1 to 20 ± 5 km) within 50 km of the InSight lander. The mid-crust is one of four robust seismically detectable kilometer-scale layers beneath InSight (10–13) and may be global (8). V_p and layer thickness have been challenging to obtain for other locations on Mars (see ref. 9 and references therein). Temperatures on present-day Mars become warm enough for stable liquid water near the top of mid-crust (15), and pores are expected to have closed at the bottom of the layer (16). We use Bayesian inversion and a Markov chain Monte Carlo (MCMC) algorithm (17) to identify combinations of six lithologic parameters (pore shape aspect ratio α, porosity ϕ, liquid water saturation γ_w, mineral bulk modulus κ_m, mineral shear modulus μ_m, mineral density ρ_m, Table 2) that best reproduce the three observed data points V_p, V_s, and ρ_b (Table 1). Calculations combine the seismic velocity equations, the Berryman self-consistent rock physics model (18), and the Gassmann–Biot equations (19) (*Materials and Methods*). A mid-crust composed of igneous rock with thin fractures filled with liquid water can best explain the geophysical data.

Results and Discussion

Fig. 1 summarizes inversion results when the MCMC algorithm samples a range of mineral moduli and densities spanning from mafic (14, 20) to more evolved igneous rocks (14, 21) represented by a range between 100% basalt and 100% plagioclase. Several combinations of parameters produce good fits to the observed V_p, V_s, and ρ_b data within assumed errors (Fig. 1 *V–X*). α, ϕ, μ_m, and γ_w are well resolved. A fully liquid water-saturated crust $\gamma_w = 100\%$ is most probable (Fig. 1F); ϕ is estimated as 0.17 ± 0.07 (Fig. 1C) and

Author affiliations: [a]Scripps Institution of Oceanography, University of California San Diego, La Jolla, CA 92093; and [b]Department of Earth and Planetary Science, University of California Berkeley, Berkeley, CA 94720

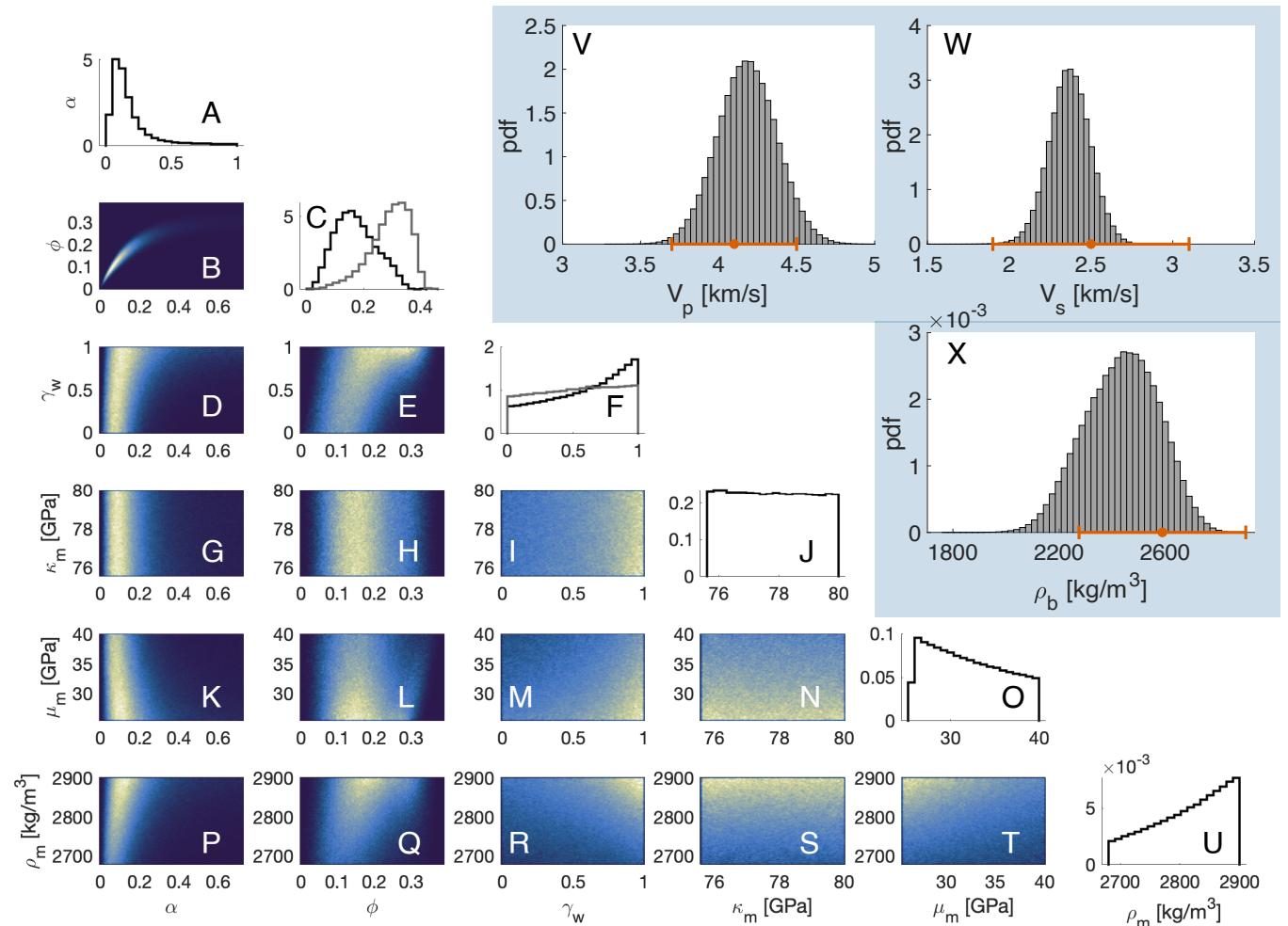[1]To whom correspondence may be addressed. Email: vwright@ucsd.edu.

Fig. 1. Summary of inversion results. Panels (*A–U*): Histograms of marginal posterior distributions of model parameters, computed from 5×10^5 iterations of the MCMC (17). The area under each histogram is equal to one. In the 2D histograms, cold colors (blues) indicate low posterior probability, and warm colors (yellows and whites) indicate regions of high posterior probability. In the 1D histograms, black stair plots show results for our default parameters bounds (Table 2). The light gray stair plots in panels (*C*) and (*F*) illustrate results obtained with widened bounds on mineralogical parameters (*Results and Discussion*). Water content is nearly uniformly distributed (*F*) under these assumptions, but the porosity takes on unreasonably large values (0.29 ± 0.07). Panels (*A*) and (*C*) show that α and ϕ are tightly constrained by the data. Panel (*B*) reveals a nonlinear relationship between ϕ and α. Panel (*F*) indicates that a high water saturation is likely in view of the data. Panel (*J*) shows that κ_m is not constrained by the data. Panels (*V–X*): Data fits. Histograms show model responses (V_p, V_s, and ρ_b) for each of the parameters in panels (*A–U*), normalized so that the area under the graph is one. The orange error bars (horizontal) illustrate the mean of the data (filled dot) and expected errors (two SD).

α as 0.19 ± 0.18 (Fig. 1*A*), implying thin fractures. The inversion recovers a nonlinear relationship between α and ϕ (Fig. 1*B*). κ_m is not well-constrained by the data (Fig. 1*K*).

We explored the robustness of the result above by expanding the mineral parameter bounds the MCMC explores: $\rho_m = 2,680-4,250$ kg/m^3, $\kappa_m = 75.6-107.6$ GPa, and $\mu_m = 25.6-76.8$ GPa. $\gamma_w = 100\%$ remains most probable until the MCMC explores $\rho_m > 4,000$ kg/m^3. $\gamma_w = 0-100\%$ becomes nearly equally probably beyond this (Fig. 1*F*), also resulting in $\phi = 0.29 \pm 0.07$ (Fig. 1*C*) and $\rho_m = 3,702 \pm 363$ kg/m^3. This latter solution is inconsistent with independent observations: i) $\phi = 0.29 \pm 0.07$ is larger than the mean ϕ of the crust (0.1 to 0.23) (22, 23) and dense (>3,100 kg/m^3) Martian meteorites (~0.1, with values typically <0.23) (24); ii) ϕ at the surface is 0.3 to 0.5 (25, 26) and should substantially decrease at mid-crustal depths, with pores closing at 20 km as discussed in refs. 7, 14, 16, 23, and 26.

A mid-crust containing liquid water has implications for the Martian water budget and hydrological cycle. Assuming the

InSight location as representative, motivated by similar V_p/V_s (1.81 to 1.98) and seismically derived ϕ (0.1 to 0.17) (8) beneath InSight and areas up to 4,500 km away from the lander, 10 km of crust with porosity of 0.1 to 0.2 translates to 1 to 2 km of water—more than the water volumes proposed to have filled

Table 1. Geophysical data for the mid-crust beneath the InSight lander

Source	V_p (km/s)	V_s (km/s)	ρ_b (kg/m^3)
Knapmeyer-Endrun et al. (10)	—	2.3 ± 0.3	—
Duran et al. (11)	—	2.5 to 3.3	—
Carrasco et al. (12)	3.75 to 4.55	2.0 to 2.5	—
Joshi et al. (13)	—	2.3 to 2.6	—
Derived from refs. 14, 26, and 27	—	—	2,589 ± 157

See *Materials and Methods* for ρ_b calculations, which assume crustal mineralogies ranging between 100% plagioclase and 100% basalt.

Table 2. Model parameters (7) explored in the inversion

Parameters	Ranges
Pore shape aspect ratio (α)	0.03 to 0.99
Porosity (ϕ)	0.05 to 0.50
Water saturation (γ_w) (%)	0 to 100
Mineral bulk modulus (κ_m) (GPa)	76.5 to 80
Mineral shear modulus (μ_m) (GPa)	25.6 to 40
Mineral density (ρ_m) (kg/m^3)	2,689 to 2,900

hypothesized ancient Martian oceans (2). Thus, Mars' crust need not have lost most of its water via atmospheric escape. Liquid water in the pores of the mid-crust also requires high enough permeability and warm enough temperatures in the shallow crust to permit exchange between the surface and greater depths. While available data are best explained by a water-saturated mid-crust, our results highlight the value of geophysical measurements and better constraints on the mineralogy and composition of Mars' crust.

Materials and Methods

Constraining the Mid-Crustal Bulk Density. The bulk density of the mid-crust has not been directly constrained by the gravity, seismic velocity, and mineralogical data used to derive the average bulk density and thickness of the crust beneath InSight (14). We can, however, infer the bulk density of the mid-crust using three constraints. First, the average bulk density within the upper 1.2 km is $1,600 \pm 360$ kg/m^3 and $2,300 \pm 130$ kg/m^3 between 1.2 and 11.5 km. These numbers are based on the estimated average bulk densities within the upper few hundred meters below the surface (26) and ~5 km below the surface (27) of the adjacent Gale Crater on Mars. Second, the bulk density of the crust increases with depth (22). Third, the bulk density of the layer beneath 20 km $\pm$ 5 km is the same as its mineral density due to pore-closure (16). An average bulk density of the mid-crust can be obtained by solving a constrained problem to reproduce the average bulk density of the crust, $2,580 \pm 209$ kg/m^3 (14).

Rock Physics Models. Seismic velocities V_p and V_s depend on bulk density ρ_b and effective shear μ_e and bulk κ_e moduli:

$$V_p = ((\kappa_e + (4/3)\mu_e)/\rho_b)^{1/2}, \quad V_s = (\mu_e/\rho_b)^{1/2} \quad [1]$$

Berryman's rock physics model (18) provides dry-frame shear μ_d and bulk κ_d moduli of fractured rocks [see ref. 7 for a list of Berryman's equations (18)]. The model uses a self-consistent approach and long-wavelength scattering theory that allows inclusions to overlap (18). Model inputs are ϕ, κ_m, μ_m, ρ_m, and α. $\mu_e = \mu_d$ (19).

We use Gassmann–Biot fluid substitution theory (19) to estimate κ_e from κ_d, ϕ, κ_m, and the bulk moduli of the fluid in a dry ($\kappa_{f1} = 0$ kPa for gas) versus partially to fully liquid-saturated (κ_{f2}) rock,

$$\frac{\kappa_e}{\kappa_m - \kappa_e} - \frac{\kappa_{f2}}{\phi(\kappa_m - \kappa_{f2})} = \frac{\kappa_d}{\kappa_m - \kappa_d} + \frac{\kappa_{f1}}{\phi(\kappa_m - \kappa_{f1})}. \quad [2]$$

With constraints on μ_e and κ_e from Berryman and Gassmann–Biot equations (18, 19), we then estimate V_s and V_p via Eq. 1.

Bayesian Inversion. We perform a Bayesian inversion, which requires that we specify a prior $p_0(x)$ and a likelihood $p_l(y|x)$, where x are the six unknown parameters that we invert for (α, ϕ, γ_w, κ_m, μ_m, and ρ_m, which control κ_e, μ_e, and ρ_b) and

$$y = (4.1 \text{ km/s}, 2.5 \text{ km/s}, 2,589 \text{ kg/m}^3), \quad [3]$$

are the three data (V_p, V_s, and ρ_b) we seek to explain. The prior is a uniform distribution over the parameter bounds in Table 2, combined with the constraint that $V_p > V_s$. The likelihood follows from assuming Gaussian errors in the data

$$p(y|x) \propto \exp\left(-0.5\|W(y - m(x))\|_2^2\right), \quad [4]$$

where $m(x)$ is the rock physics model (i.e., the forward model) and where W is a diagonal matrix whose diagonal elements are the reciprocals of the standard deviations of the data ($\sigma_{V_p} = 0.2$ km/s, $\sigma_{V_s} = 0.3$ km/s, $\sigma_{\rho_b} = 157$ kg/m^3, derived from Table 1 to render all reported data points as likely). Jointly, the prior and likelihood define a Bayesian posterior distribution, $p(x|y) \propto p_0(x)p_l(y|x)$, which we sample via an affine invariant MCMC ensemble sampler (17). Sensitivity analyses confirm that water saturation does not significantly influence V_s (19) and most strongly influences the V_p, followed by ρ_b (18).

1. V. R. Baker, Geomorphological evidence for water on Mars. *Elements* **2**, 139–143 (2006).
2. S. M. Clifford, T. J. Parker, The evolution of the Martian hydrosphere: Implications for the fate of a primordial ocean and the current state of the northern plains. *Icarus* **154**, 40–79 (2001).
3. M. H. Carr, Formation of Martian flood features by release of water from confined aquifers. *J. Geophys. Res. Solid Earth* **84**, 2995–3007 (1979).
4. B. M. Jakosky, Atmospheric loss to space and the history of water on Mars. *Annu. Rev. Earth Planet. Sci.* **49**, 71–93 (2021).
5. E. Scheller, B. Ehlmann, R. Hu, D. Adams, Y. Yung, Long-term drying of Mars by sequestration of ocean-scale volumes of water in the crust. *Science* **372**, 56–62 (2021).
6. V. Wright, J. Dasent, R. Kilburn, M. Manga, A minimally cemented shallow crust beneath InSight. *Geophys. Res. Lett.* **49**, e2022GL099250 (2022).
7. R. Kilburn, J. Dasent, V. Wright, M. Manga, Lithology, pore-filling media, and pore closure depth beneath InSight on Mars inferred from shear wave velocities. *J. Geophys. Res.: Planets* **127**, e2022JE007539 (2022).
8. J. Li et al., Constraints on the Martian crust away from the insight landing site. *Nat. Commun.* **13**, 7950 (2022).
9. P. Lognonné et al., Mars seismology. *Annu. Rev. Earth Planet. Sci.* **51**, 643–670 (2023).
10. B. Knapmeyer-Endrun et al., Thickness and structure of the Martian crust from InSight seismic data. *Science* **373**, 438–443 (2021).
11. C. Duran et al., Seismology on Mars: An analysis of direct, reflected, and converted seismic body waves with implications for interior structure. *Phys. Earth Planet. Inter.* **325**, 106851 (2022).
12. S. Carrasco et al., Constraints for the Martian crustal structure from Rayleigh waves ellipticity for large seismic events. *Geophys. Res. Lett.* **50**, e2023GL104816 (2023).
13. R. Joshi et al., Joint inversion of receiver functions and apparent incidence angles to determine the crustal structure of Mars. *Geophys. Res. Lett.* **50**, e2022GL100469 (2023).
14. M. A. Wieczorek et al., InSight constraints on the global character of the Martian crust. *J. Geophys. Res.: Planets* **127**, e2022JE007298 (2022).

15. S. Clifford et al., Depth of the Martian cryosphere: Revised estimates and implications for the existence and detection of subpermafrost groundwater. *J. Geophys. Res.: Planets* **115**, E07001 (2010).
16. S. Gyalay, F. Nimmo, A. C. Plesa, M. Wieczorek, Constraints on thermal history of Mars from depth of pore closure below InSight. *Geophys. Res. Lett.* **47**, e2020GL088653 (2020).
17. J. Goodman, J. Weare, Ensemble samplers with affine invariance. *Commun. Appl. Math. Comput. Sci.* **5**, 65–80 (2010).
18. J. G. Berryman, Long-wavelength propagation in composite elastic media. I. Spherical inclusions & II. Ellipsoidal inclusions. *J. Acoust. Soc. Am.* **68**, 1820–1831 (1980).
19. M. A. Biot, Theory of propagation of elastic waves in a fluid-saturated porous solid. II. Higher frequency range. *J. Acoust. Soc. Am.* **28**, 179–191 (1956).
20. M. Golombek et al., Geology of the InSight landing site on Mars. *Nat. Commun.* **11**, 1–11 (2020).
21. J. R. Michalski, A. Deanne Rogers, C. S. Edwards, A. Cowart, L. Xiao, Diverse volcanism and crustal recycling on early Mars. *Nat. Astron.* **8**, 456–462 (2024).
22. S. Goossens et al., Evidence for a low bulk crustal density for Mars from gravity and topography. *Geophys. Res. Lett.* **44**, 7686–7694 (2017).
23. J. Li et al., Evidence for crustal seismic anisotropy at the InSight lander site. *Earth Planet. Sci. Lett.* **593**, 117654 (2022).
24. D. T. Britt, G. Consolmagno, Stony meteorite porosities and densities: A review of the data through 2001. *Meteor. Planet. Sci.* **38**, 1161–1180 (2003).
25. P. Lognonné et al., Constraints on the shallow elastic and anelastic structure of Mars from InSight seismic data. *Nat. Geosci.* **13**, 213–220 (2020).
26. K. W. Lewis et al., A surface gravity traverse on Mars indicates low bedrock density at Gale crater. *Science* **363**, 535–537 (2019).
27. B. Johnson, R. Milliken, K. Lewis, G. Collins, Impact generated porosity in Gale crater and implications for the density of sedimentary rocks in lower Aeolis Mons. *Icarus* **366**, 114539 (2021).